

**Controlling stoichiometry in ultrathin van der Waals films: PtTe<sub>2</sub>, Pt<sub>2</sub>Te<sub>3</sub>, Pt<sub>3</sub>Te<sub>4</sub>, and Pt<sub>2</sub>Te<sub>2</sub>**

Lasek, K.; Ghorbani Asl, M.; Pathirage, V.; Krasheninnikov, A.; Batzill, M.;

Originally published:

June 2022

**ACS Nano 16(2022), 9908-9919**

DOI: <https://doi.org/10.1021/acsnano.2c04303>

Perma-Link to Publication Repository of HZDR:

<https://www.hzdr.de/publications/Publ-35053>

Release of the secondary publication  
on the basis of the German Copyright Law § 38 Section 4.

# Controlling stoichiometry in ultrathin van der Waals films: PtTe<sub>2</sub>, Pt<sub>2</sub>Te<sub>3</sub>, Pt<sub>3</sub>Te<sub>4</sub>, and Pt<sub>2</sub>Te<sub>2</sub>

Kinga Lasek,<sup>1</sup> Mahdi Ghorbani-Asl,<sup>2</sup> Vimukthi Pathirage,<sup>1</sup> Arkady V Krasheninnikov,<sup>2,3</sup> Matthias Batzill<sup>1,\*</sup>

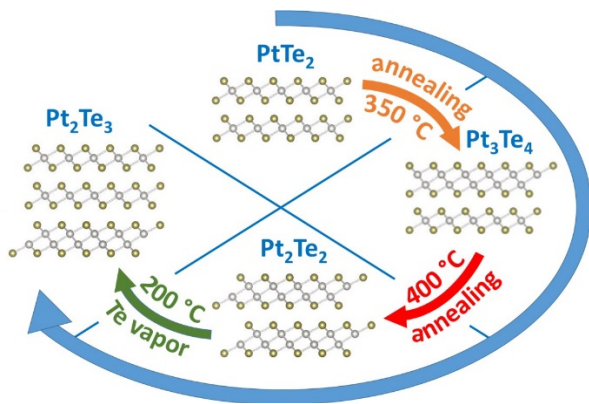
<sup>1</sup> Department of Physics, University of South Florida, Tampa, FL 33620, USA

<sup>2</sup> Helmholtz-Zentrum Dresden-Rossendorf, Institute of Ion Beam Physics and Materials Research, 01328 Dresden, Germany

<sup>3</sup> Department of Applied Physics, Aalto University, P.O. Box 11100, 00076 Aalto, Finland

\* Corresponding author: Matthias Batzill; e-mail: mbatzill@usf.edu

## TOC-figure:



**Abstract:**

The platinum-tellurium phase diagram exhibits various (meta)stable van der Waals (vdW) materials, that can be constructed by stacking PtTe<sub>2</sub> and Pt<sub>2</sub>Te<sub>2</sub> layers. Mono phase PtTe<sub>2</sub>, being the thermodynamically most stable compound, can readily be grown as thin films. Obtaining the other phases (Pt<sub>2</sub>Te<sub>3</sub>, Pt<sub>3</sub>Te<sub>4</sub>, Pt<sub>2</sub>Te<sub>2</sub>), especially in their ultimate thin form, is significantly more challenging. We show that PtTe<sub>2</sub> thin films can be transformed by vacuum annealing-induced Te-loss into Pt<sub>3</sub>Te<sub>4</sub>- and Pt<sub>2</sub>Te<sub>2</sub>- bilayers. These transformations are characterized by scanning tunneling microscopy, x-ray and angle resolved photoemission spectroscopy. Once Pt<sub>3</sub>Te<sub>4</sub> is formed, it is thermally stable up to 350°C. To transform Pt<sub>3</sub>Te<sub>4</sub> into Pt<sub>2</sub>Te<sub>2</sub>, a higher annealing temperature of 400°C is required. The experiments combined with density functional theory calculations provide insights into these transformation mechanisms and show that a combination of the thermodynamic preference of Pt<sub>3</sub>Te<sub>4</sub> over a phase segregation into PtTe<sub>2</sub> and Pt<sub>2</sub>Te<sub>2</sub> and an increase in the Te-vacancy formation energy for Pt<sub>3</sub>Te<sub>4</sub> compared to the starting PtTe<sub>2</sub> material is critical to stabilize the Pt<sub>3</sub>Te<sub>4</sub> bilayer. To desorb more tellurium from Pt<sub>3</sub>Te<sub>4</sub> and transform the material into Pt<sub>2</sub>Te<sub>2</sub>, a higher Te-vacancy formation energy has to be overcome by raising the temperature. Interestingly, bilayer Pt<sub>2</sub>Te<sub>2</sub> can be re-tellurized by exposure to Te-vapor. This causes the selective transformation of the topmost Pt<sub>2</sub>Te<sub>2</sub> layer into two layers of PtTe<sub>2</sub>, and consequently the synthesis of e Pt<sub>2</sub>Te<sub>3</sub>. Thus, all known Pt-telluride vdW compounds can be obtained in their ultrathin form by carefully controlling the stoichiometry of the material.

**Keywords:** van der Waals materials; 2D materials; interlayer interaction; charge transfer; phase stability; platinum telluride; composition control.

Layered transition (or post-transition) metal chalcogenides as mono- or few-layer materials have recently received enormous amount of attention due to their special properties.<sup>1</sup> Specifically, the Pt-tellurides have many attractive attributes that allow us to gain better fundamental understanding of van der Waals (vdW) materials and their potential applications. The Pt-tellurides have attracted interest for: (i) layer dependent electronic properties that cause opening of a band gap in monolayer PtTe<sub>2</sub>, while the system otherwise is (semi)metallic,<sup>2,3,4,5,6</sup> (ii) topological features<sup>7,8</sup> for both PtTe<sub>2</sub> and Pt<sub>3</sub>Te<sub>4</sub> and a strong spin texture that unlike the topological states persist down to the monolayer, making them potentially interesting materials for spintronics applications,<sup>9,10</sup> and (iii) useful electrochemical properties for hydrogen evolution as well as oxygen reduction reactions.<sup>11,12,13,14</sup>

While most of the layered chalcogenides exist in a single preferred composition, typically as di-chalcogenides<sup>1</sup> or mono-chalcogenides,<sup>15,16,17</sup> platinum tellurides are the only transition metal chalcogenides that can be found as both mono- and di-chalcogenide vdW materials. Minerals of Pt tellurides are known to form di-tellurides with one metal atom sandwiched between tellurium atoms<sup>18,19</sup> or mono-telluride<sup>20,21</sup> with two platinum atoms sandwiched between tellurium atoms. In addition, phases consisting of alternating layers of di-telluride and mono-tellurides are known to also exist.<sup>22</sup> For instance, structures with alternating layers of PtTe<sub>2</sub> and Pt<sub>2</sub>Te<sub>2</sub>\* occur that have an overall composition of Pt:Te of 3:4.<sup>23</sup> These phases have also been synthesized as bulk crystals.<sup>7</sup> Moreover, the alternating stacking of *two* PtTe<sub>2</sub> layers and *one* Pt<sub>2</sub>Te<sub>2</sub> layer, *i.e.*, a material with a composition of Pt<sub>2</sub>Te<sub>3</sub>, is known to be a stable configuration.<sup>22</sup> Thus, this implies the existence of at least four distinct vdW compounds of Pt-telluride, which makes this system particularly interesting in the context of engineering properties by controlling the stoichiometry of this compound. Specifically, the strong spin momentum locking in both PtTe<sub>2</sub> and Pt<sub>3</sub>Te<sub>4</sub> (Pt<sub>2</sub>Te<sub>3</sub> and Pt<sub>2</sub>Te<sub>2</sub> has not been studied yet) makes these materials potentially suitable for spin-torque devices or spin-injection and spin-detection devices.<sup>17,24</sup> However, for the fabrication of

---

\* To better reflect the presence of single and double metal layer in the material, we write the composition of these materials as MX<sub>2</sub> and M<sub>2</sub>X<sub>2</sub> (M=metal and X=chalcogen) for the di-chalcogenides and mono-chalcogenides, respectively.

such devices, thin films are required and thus processes must be developed that enable robust materials synthesis of Pt-telluride with controlled composition.<sup>4</sup>

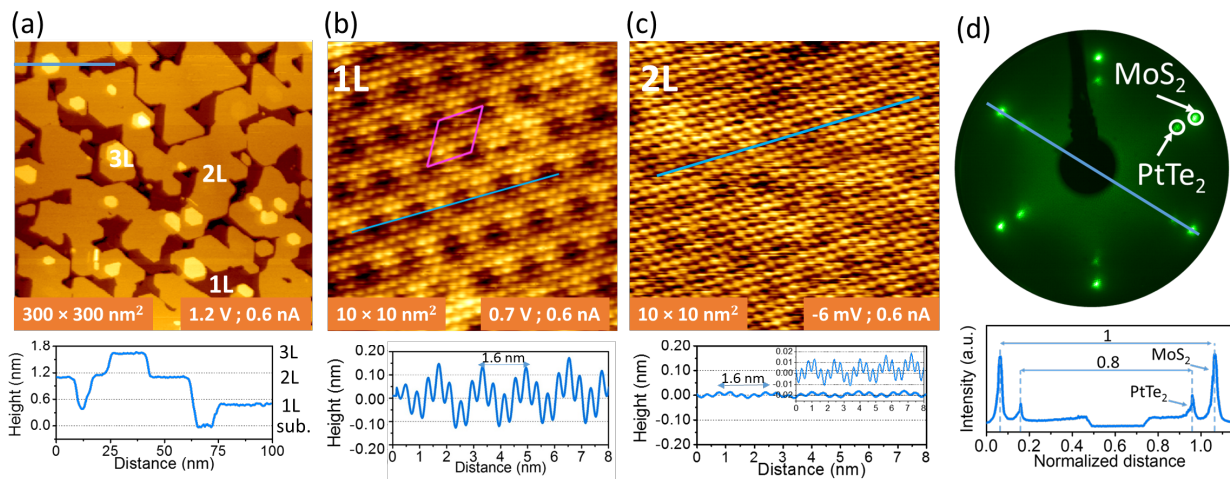
For the synthesis of bulk materials, the composition may be effectively controlled by sealing the starting material in a precise mixture. However, the synthesis of Pt mono-telluride ( $\text{Pt}_2\text{Te}_2$ ) has been demonstrated to be still problematic due to unfavorable thermodynamic stability.<sup>4</sup> Compositional control in high quality ultrathin 2D films is even more challenging. The high vapor pressure of tellurium requires an excess tellurium flux for telluride thin film growth, which makes a compositional control of a film by tuning the flux ratios during deposition in most cases impracticable. Consequently, a different approach must be used to control the amount of tellurium in the film.

Here we show that starting with  $\text{PtTe}_2$  films, other compositions can be obtained by a post-growth desorption of tellurium from the film. We demonstrate that this process allows to synthesize the intermediate mixed phase with its minimum thickness (the minimum thickness of  $\text{Pt}_3\text{Te}_4$  consisting of one  $\text{PtTe}_2$ - and one  $\text{Pt}_2\text{Te}_2$ - layer, *i.e.*, is a bilayer vdW structure). Moreover, bilayer Pt-monotelluride ( $\text{Pt}_2\text{Te}_2$ ) can also be obtained by further desorption of tellurium. Interestingly, once  $\text{Pt}_2\text{Te}_2$  bilayers are formed, the top surface layer can be re-tellurized by exposure to Te-vapor, which then forms two  $\text{PtTe}_2$  layers on top of a  $\text{Pt}_2\text{Te}_2$  layer and thus we achieve the  $\text{Pt}_2\text{Te}_3$  structure in its thinnest trilayer form. All the growths and transformations are studied by scanning tunneling microscopy (STM) and photoemission spectroscopy, giving detailed information on the transformation processes. Density functional theory (DFT) simulations draw a picture of a delicate interplay between thermodynamic phase stability and Te-vacancy formation energies that enable the synthesis of the different phases.

## Results and Discussion

*Film morphology:*  $\text{PtTe}_2$  ultrathin films are grown by vdW-epitaxy on  $\text{MoS}_2$  single crystal substrates by vacuum co-deposition of Pt and Te. The as grown  $\text{PtTe}_2$  ultrathin films consist of monolayer and bilayer islands with some bare  $\text{MoS}_2$ -substrate remaining. In addition, some rare

PtTe<sub>2</sub> tri-layer<sup>†</sup> islands are also visible in the large-scale STM images shown in Fig. 1(a). Zooming in on the monolayer regions, a moiré structure is observed, as shown in Fig. 1(b). The 4×4 periodicity of the PtTe<sub>2</sub> moiré structure agrees well with a close-to-coincidence structure with the MoS<sub>2</sub> substrate, *i.e.*, five times the lattice constant of MoS<sub>2</sub> ( $a_{\text{MoS}_2} = 0.316 \text{ nm}$ )<sup>25</sup> is close to four times the lattice constant of PtTe<sub>2</sub> with  $a_{\text{PtTe}_2} = 0.4 \text{ nm}$ , which was estimated from low energy electron diffraction (LEED) measurements presented in Fig. 1(d). This experimental value for the lattice constant is also in agreement with the lattice constant calculated by our DFT calculations of the relaxed structure for monolayer PtTe<sub>2</sub> of 0.398 nm. The appearance of the moiré structure is strongly bias voltage dependent in STM images (see supporting information Fig. S1) with only clear contrast at voltages below 0.8 V and no contrast for higher voltages. The bias voltage dependence of the moiré structure suggests that the observed corrugation in STM is partially due to an electronic contrast indicating locally varying interactions within the moiré unit cell of the MoS<sub>2</sub>/PtTe<sub>2</sub> van der Waals heterostructure. While the moiré structure is most pronounced for the monolayer, it does persist for bilayer islands, however, with a much weaker corrugation. Nevertheless, this persistence of moiré structures into the bilayer indicates strong coupling between the first- and second- van der Waals-layer. Fig. 1(c) shows the moiré-structure for the bilayer acquired at a very low bias voltage.



<sup>†</sup> In this manuscript, a layer is defined as a vdW-layer, *i.e.*, a structural unit which is separated from the next unit by a vdW gap.

*Figure 1: Scanning tunneling microscopy images of the as grown PtTe<sub>2</sub> on a MoS<sub>2</sub> substrate. (a) Large scale STM image showing predominantly islands with a height corresponding to bilayer structures, labeled as 2L, some monolayer islands (labeled 1L) and trilayer islands (labeled 3L) are also observed. The line scan shows the MoS<sub>2</sub> substrate at 0 nm height and the corresponding heights of monolayer, bilayer, and tri-layer height islands. (b) High resolution image of a monolayer region, showing a 4 × 4 moiré structure with 1.6 nm periodicity as evident from the line scan presented below. (c) High resolution image of bilayer region. The moiré pattern is still faintly visible at very low bias voltages. (d) The LEED pattern has been measured on the as grown bilayer thick film, with a primary electron energy of E<sub>K</sub> = 48 eV. The lattice constant of PtTe<sub>2</sub> film is measured by using the MoS<sub>2</sub> substrate diffraction spots as a reference.*

Post-growth vacuum annealing of PtTe<sub>2</sub> ultrathin films results in changes of the sample morphology. In large-scale STM images mono-layer islands disappear and the film converts to almost entirely bi-layer PtTe<sub>2</sub> with bare MoS<sub>2</sub> substrates in the areas between the PtTe<sub>2</sub> islands, as shown in Fig. 2. This indicates that bilayers are favored over monolayers and that atom-mobility is high enough at the annealing temperatures of 350 °C to rearrange monolayer regions into bilayers. For longer annealing tri-layer islands also disappear. With longer annealing time and annealing to higher temperature, the overall coverage of the sample with bi-layer Pt-telluride decreases as shown in Fig. 2. This decrease in surface coverage is consistent with the formation of more Pt-dense layers, i.e., a conversion of PtTe<sub>2</sub> towards Pt<sub>2</sub>Te<sub>2</sub> (see XPS analysis below). The annealing is conducted at two annealing temperatures. After a total annealing time of ~ 200 min at 350 °C, a plateau for the bilayer surface coverage is reached, which remains roughly constant at this annealing temperature even after annealing for 450 min. However, raising the annealing temperature slightly to 400 °C causes a further decrease in surface coverage. The change in the surface morphology for some representative annealing steps can be seen from the corresponding large-scale STM images shown in Fig. 2.

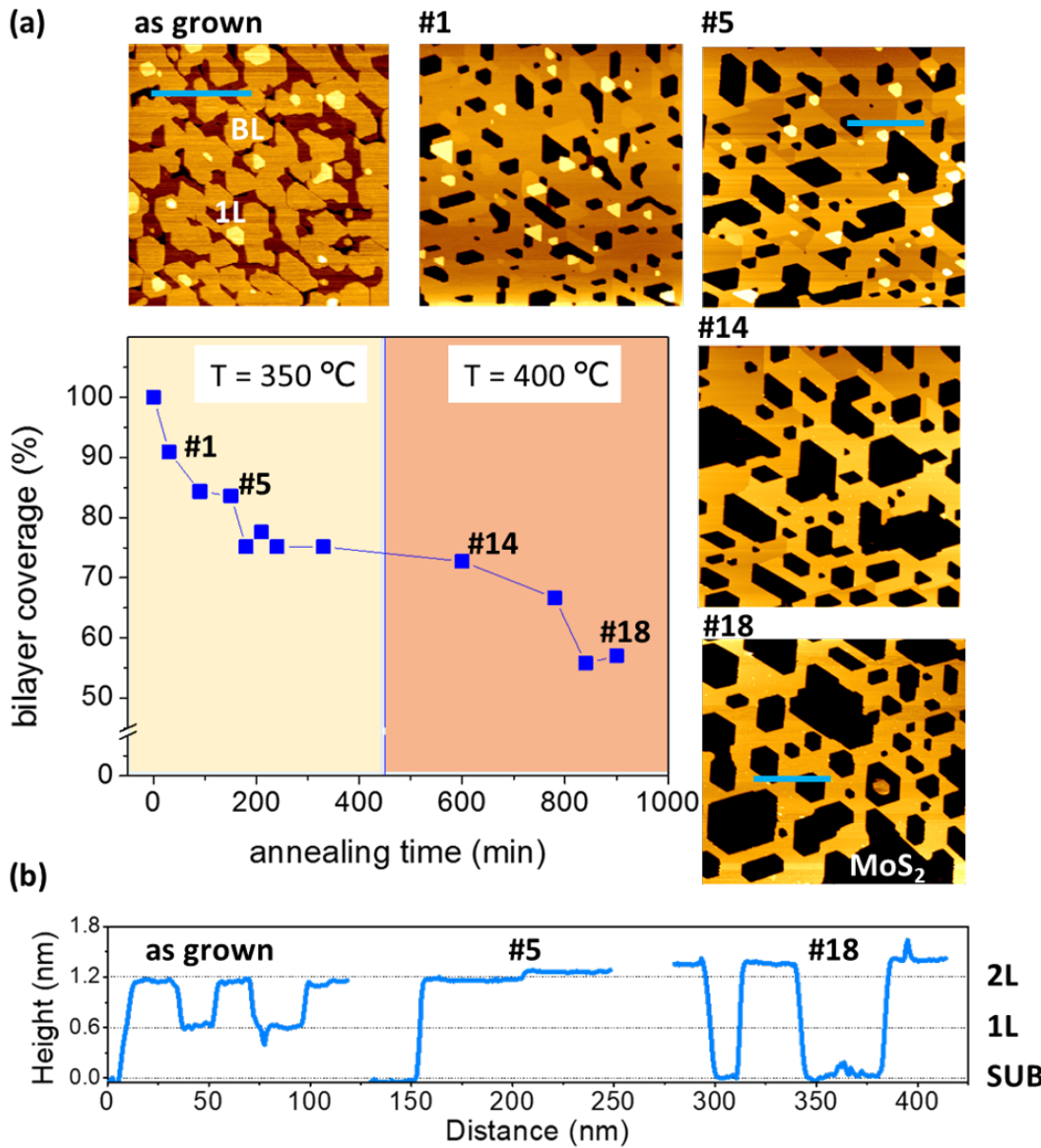


*Figure 2: STM analysis of surface coverage with bilayer Pt-tellurides as a function of annealing temperature and time. (a) Initial annealing at 350 °C causes a decrease of the surface coverage that plateaus after annealing for about 200 min. Annealing at 400 °C causes a further decrease in the bilayer coverage. The annealing steps are consecutively numbered and some representative STM images for specific annealing steps are shown. Note that the contrast variation that can be seen on the bilayer regions indicates different Pt-telluride phases, which is discussed below in more detail. (b) Selected line profiles from the STM images shown in (a).*

*X-ray photoemission spectroscopy (XPS):* To understand morphology changes observed in STM, the compositional change and chemical shifts that indicate the formation of different phases are analyzed by XPS as a function of annealing temperature. XPS analysis is shown in Fig. 3. Tellurium is lost from the sample and another phase with a distinct Pt-4f core level position is formed. The Te-3d to Pt-4f peak ratio as a function of annealing is shown in Fig. 3(a). Here we normalized the Te-3d/Pt-4f intensity ratio to 2, for the as grown sample. This normalization allows us to compare the ratios directly to the atomic ratios of the film, *i.e.*, we postulate that the as grown sample is close to  $\text{PtTe}_2$ . This is justified from core-level peak positions and ARPES studies discussed below. Like the change observed in the STM images, a plateau is reached for the Te-3d/Pt-4f intensity ratio after annealing for about 200 min at 350 °C. The normalized intensity ratio of this plateau is close to 1.3, *i.e.* an atomic composition of Te:Pt= 4:3 suggesting a  $\text{Pt}_3\text{Te}_4$  compound. Further annealing at 400 °C causes an additional reduction of the normalized Te:Pt ratio reaching a value of ~1, *i.e.*, consistent with a  $\text{Pt}_2\text{Te}_2$  compound.

The changes to different compositional phases with annealing can also be observed from analyzing chemical shifts in the Pt-4f core levels and the respective ratio of the components associated with these different phases. Fig. 3(b) shows the Pt-4f peak for three distinct annealing temperatures. For the as grown  $\text{PtTe}_2$  sample the Pt-4f peak can be fitted with a single doublet at binding energy of 76.2 eV for  $\text{Pt-4f}_{5/2}$ . Similarly, after annealing at 400 °C for a prolonged time a single doublet describes the Pt-4f core level peak, with a  $\text{Pt-4f}_{5/2}$  peak at 75.0 eV binding energy. This binding energy is assigned to a  $\text{Pt}_2\text{Te}_2$  phase based on the measured Te:Pt ratio. The Pt-4f peak that is obtained in the intermediate plateau region, *i.e.*, after annealing to 350 °C for more than 200 min, can only be fit reasonably with two doublets, indicating Pt-atoms in two different chemical environments. Such two different environments are consistent with the  $\text{Pt}_3\text{Te}_4$  phase that comprises alternating  $\text{PtTe}_2$  and  $\text{Pt}_2\text{Te}_2$  layers. Thus, as a first approximation one may expect that these two doublets have the same binding energies as the pure  $\text{PtTe}_2$  and the pure  $\text{Pt}_2\text{Te}_2$  phases. Indeed, by fitting using the same peak shapes as those found for the ‘pure’ phases but allowing for the peak position to adjust, we find that the binding energy for the two components are close to those of the pure phases. The  $\text{Pt}_2\text{Te}_2$  component is unchanged as compared to that

of the pure  $\text{Pt}_2\text{Te}_2$  phase, while there is a small but significant shift of  $\sim 0.3$  eV to lower binding energy for the  $\text{Pt}\text{Te}_2$  component as compared to pure  $\text{Pt}\text{Te}_2$ . This shift may be associated with a change in the electronic structure in  $\text{Pt}_2\text{Te}_2/\text{Pt}\text{Te}_2$  heterostructure compared to the pure  $\text{Pt}\text{Te}_2$  phase and is an indication that the  $\text{Pt}_2\text{Te}_2/\text{Pt}\text{Te}_2$  heterolayer, *i.e.*, the  $\text{Pt}_3\text{Te}_4$  phase, has distinct properties from those of the  $\text{Pt}_2\text{Te}_2$  and  $\text{Pt}\text{Te}_2$  phases. Detailed electronic structure characterization of the different phases is discussed below by angle resolve photoemission spectroscopy (ARPES) measurements. A complete set of XPS Pt-4f and Te-3d peaks are presented in the supplemental information in Fig. S2 and S3.

The presence of two components in the Pt-4f peak associated with Pt in a  $\text{Pt}_2\text{Te}_2$  and  $\text{Pt}\text{Te}_2$  environment enables us to plot the ratio of these two components as a function of annealing temperature and time as shown in Fig. 3(c). Again, we observe the same plateauing for annealing times of longer than 200 min at  $350^\circ\text{C}$ . At the plateau, the two chemically distinct components of the Pt-4f peak have a ratio of close to 2 to 1, which is expected for a  $\text{Pt}_3\text{Te}_4$  bilayer consisting of one  $\text{Pt}\text{Te}_2$  and one  $\text{Pt}_2\text{Te}_2$  layer (note that there are twice as many Pt-atoms in the  $\text{Pt}_2\text{Te}_2$  vdW-layer than in the  $\text{Pt}\text{Te}_2$  vdW layer). Thus, Te:Pt,  $\text{Pt}_{\text{Pt}\text{Te}_2}:\text{Pt}_{\text{Pt}_2\text{Te}_2}$ , as well as the change in the film morphology measured by STM all indicate that vacuum annealing of a  $\text{Pt}\text{Te}_2$  film at  $350^\circ\text{C}$  results in its conversion to a  $\text{Pt}_3\text{Te}_4$  bilayer, which remains stable at this annealing temperature. An increase in the annealing temperature to  $400^\circ\text{C}$  is required to increase Te-loss and convert the film further to  $\text{Pt}_2\text{Te}_2$ . Interestingly, this observation suggests that although the  $\text{Pt}_3\text{Te}_4$  phase contains a  $\text{Pt}\text{Te}_2$  vdW-layer, the  $\text{Pt}\text{Te}_2$  vdW-layer in  $\text{Pt}_3\text{Te}_4$  phase is more stable against thermal Te-desorption than in the pure  $\text{Pt}\text{Te}_2$  compound. This observation is consistent with Te-vacancy formation energies calculated by DFT and discussed below.

The time dependence with which the different phases transform at a constant annealing temperature also provide additional information on the transformation process. The transformation of  $\text{Pt}\text{Te}_2$  to  $\text{Pt}_3\text{Te}_4$  at  $350^\circ\text{C}$  may be fit by an exponential decay function with a halftime-constant between 100-110 min (see Fig. 3 (a), (c) and S4). While the time constant is dependent on the exact annealing temperature, and thus provides limited physical insight, the

fact that the transformation follows an exponential decay suggests that Te is lost at a uniform rate from the  $\text{PtTe}_2$  phase region only and desorption is suppressed from regions that have transformed to the  $\text{Pt}_3\text{Te}_4$  phase. This interpretation is supported by the thermal stability of the  $\text{Pt}_3\text{Te}_4$  phase at 350°C once the entire film is transformed to this phase. In contrast the further transformation to  $\text{Pt}_2\text{Te}_2$  at 400°C is roughly linear with time as best observed in Fig. 3(c). This suggest that Te is lost from the surface at a constant rate independent of the fraction of the different compositional phases present at the surface, *i.e.*, at 400°C Te is desorbed from both  $\text{Pt}_3\text{Te}_4$  and  $\text{Pt}_2\text{Te}_2$  at similar rates. This suggest that although  $\text{Pt}_2\text{Te}_2$  is the phase with the lowest Te-concentration it can still desorb Te at 400 °C, but lost Te may be compensated for by Te-diffusion from Te-richer phases. In addition, STM studies, discussed below, show a higher Te-vacancy concentration in the  $\text{Pt}_2\text{Te}_2$  phase compared to the other phases, indicating that replenishing of Te by diffusion from a Te-rich phases is only partially achieved. The different rates of transformation measured by XPS indicates different transformation kinetics for the transformations to different phases at different temperatures and may be correlated to the Te-vacancy formation energies for the different phases that can be computed in DFT and is discussed next.

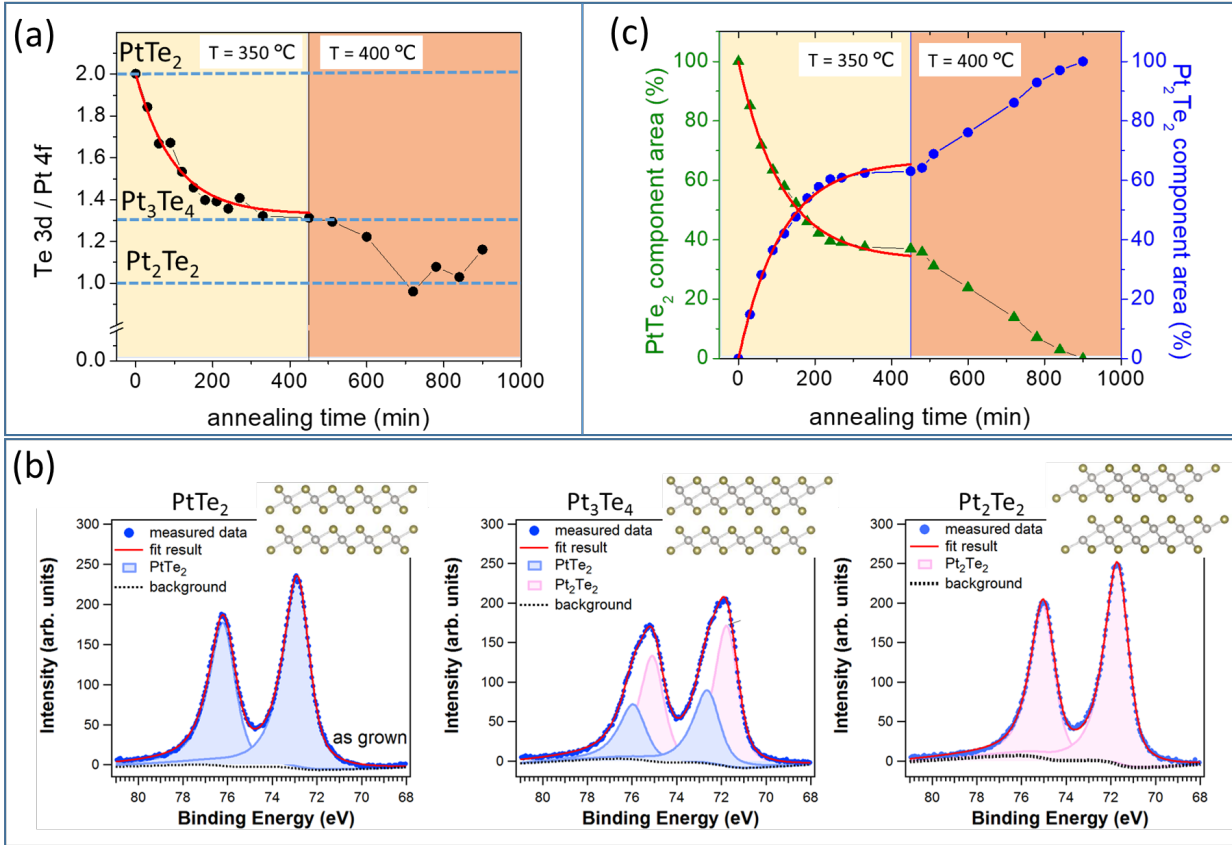


*Figure 3: XPS analysis of temperature treated Pt-telluride films. (a)* Te:Pt intensity ratio normalized to 2:1 for the as grown  $\text{PtTe}_2$  film to reflect atomic ratios. The ratios are plotted against annealing times for two annealing temperatures at initially  $350^\circ\text{C}$  that is raised to  $400^\circ\text{C}$  after 450 min. (b) Pt-4f peak for three different samples (i) as grown  $\text{PtTe}_2$ , (ii) annealed at  $350^\circ\text{C}$  for longer than 200 min, corresponding to  $\text{Pt}_3\text{Te}_4$ , and (iii) sample annealed at  $400^\circ\text{C}$  for a prolonged time, corresponding to  $\text{Pt}_2\text{Te}_2$ . (c) The two Pt-4f components (light blue and pink in (b)) corresponding to Pt in  $\text{PtTe}_2$  and  $\text{Pt}_2\text{Te}_2$  vdW-layers, respectively, are plotted as a function of annealing time and temperature. The change in the Te/Pt ratio in (a) and the percentage of the different Pt-4f components in (c) for annealing at  $350^\circ\text{C}$  is fit by an exponential decay function (red line). See Fig. S4 for fitting procedure and parameter.

*Density functional theory (DFT) considerations of the phase transformation:* In an effort to quantify some of the experimental observations that lead to the phase transformations and gain insights into the fundamental processes that enable the controlled formation of  $\text{Pt}_3\text{Te}_4$  we

conducted DFT calculations to assess the energetics of the compositional phases involved. For  $\text{Pt}_3\text{Te}_4$  to be a thermodynamically stable phase, its formation enthalpy must lie below the tie-line between  $\text{PtTe}_2$  and  $\text{Pt}_2\text{Te}_2$  phases. Otherwise, phase segregation into these two ‘pure’ phases would be thermodynamically favored. To verify this, we calculated the formation enthalpies (total energy differences) of the known vdW Pt-telluride bulk compounds. Fig. 4 (a) shows the formation enthalpies as a function of the phase compositions.  $\text{PtTe}_2$  has the lowest formation enthalpy and indeed we can find that the two possible mixed phases  $\text{Pt}_3\text{Te}_4$  and  $\text{Pt}_2\text{Te}_3$  (two  $\text{PtTe}_2$  layers alternating with one  $\text{Pt}_2\text{Te}_2$  layer) have also quite low formation enthalpies. In contrast, the formation of the layered  $\text{Pt}_2\text{Te}_2$  is significantly less favorable.

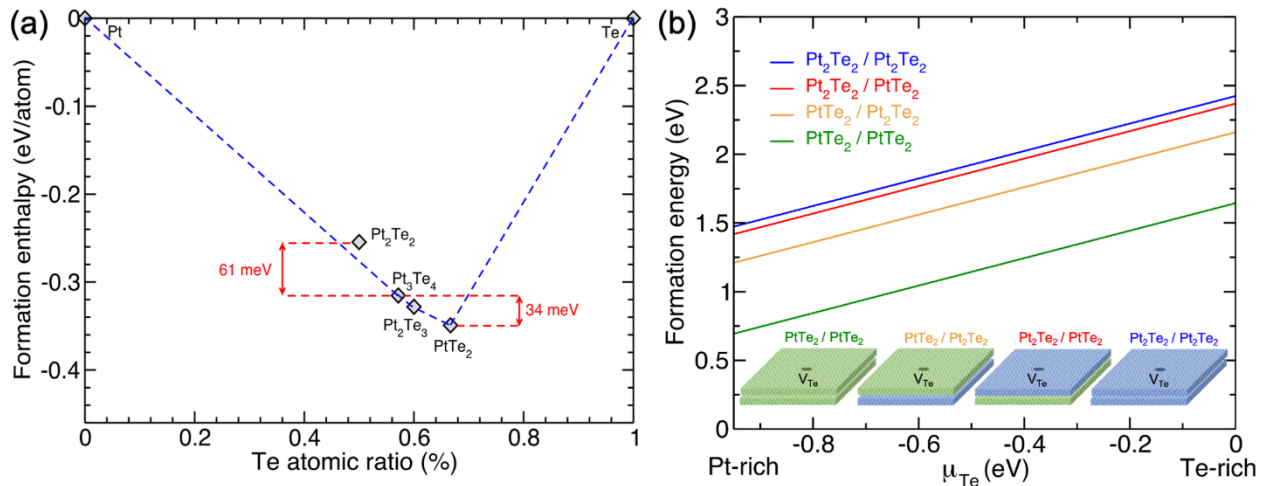


*Fig. 4. DFT energy calculations of Pt-telluride phases. (a) Calculation of the formation enthalpies of different Pt-Te phases. The blue dashed lines indicate the convex hull, with compounds lying on the convex hull being considered thermodynamic stable and phases above the convex hull are metastable. (b) Te-vacancy formation energies as a function of Te-chemical potential for four different Pt-telluride bilayer structures.*

Importantly,  $\text{Pt}_3\text{Te}_4$  is on the convex hull construction, as indicated in Fig. 4(a), while  $\text{Pt}_2\text{Te}_2$  is  $\sim 21$  meV/atom above the convex hull. This indicates that  $\text{Pt}_2\text{Te}_2$  is a metastable compound, and the material would reduce its overall energy by decomposing into pure Pt and  $\text{Pt}_3\text{Te}_4$ . This explains why  $\text{Pt}_2\text{Te}_2$  is generally difficult to synthesize. In the transformation process of the

ultrathin film, however, we are far from the thermodynamic equilibrium conditions and kinetic barriers may be important to obtain specific phases. Specifically, the formation of pure metallic Pt, even if Pt is thermodynamically favored, is likely to exhibit a nucleation barrier for the formation of metal clusters. In contrast, the structural similarity between PtTe<sub>2</sub> and Pt<sub>2</sub>Te<sub>2</sub> may facilitate the transformation of the former into the latter by addition of Pt-atoms. STM images, discussed below in more detail, show sharp phase boundaries between Pt-telluride with different compositions. Such phase boundaries exist between PtTe<sub>2</sub> to Pt<sub>3</sub>Te<sub>4</sub> as well as between Pt<sub>3</sub>Te<sub>4</sub> to Pt<sub>2</sub>Te<sub>2</sub> phases. In bilayer films, these phase boundaries can be considered as exhibiting a PtTe<sub>2</sub> to Pt<sub>2</sub>Te<sub>2</sub> contact in one of the two layers. Thus, the conversion into a phase with less tellurium consists of an expansion of a Pt<sub>2</sub>Te<sub>2</sub> layer by adding Pt into an adjacent PtTe<sub>2</sub> layer. The structural similarity between PtTe<sub>2</sub> and Pt<sub>2</sub>Te<sub>2</sub> allows this to happen without significant atom rearrangements.

The expansion of a Pt<sub>2</sub>Te<sub>2</sub> layer into a PtTe<sub>2</sub> layer may be a particularly important process for the synthesis of the thermodynamically least stable Pt<sub>2</sub>Te<sub>2</sub> phase. Formation of Pt<sub>2</sub>Te<sub>2</sub> bilayer occurs by transforming from the thermodynamically stable Pt<sub>3</sub>Te<sub>4</sub> bilayer. However, since Pt<sub>3</sub>Te<sub>4</sub> islands have both possible layer stacking with PtTe<sub>2</sub> and Pt<sub>2</sub>Te<sub>2</sub> at the top or bottom, these islands will have also in-plane contacts between PtTe<sub>2</sub> and Pt<sub>2</sub>Te<sub>2</sub> layers. This implies that in order to transform Pt<sub>3</sub>Te<sub>4</sub> into Pt<sub>2</sub>Te<sub>2</sub> no new Pt<sub>2</sub>Te<sub>2</sub> layer needs to be nucleated but only existing Pt<sub>2</sub>Te<sub>2</sub> layers need to expand into PtTe<sub>2</sub> layers. Thus, the synthesis of metastable Pt<sub>2</sub>Te<sub>2</sub> is enabled by first transforming PtTe<sub>2</sub> into the thermodynamically stable Pt<sub>3</sub>Te<sub>4</sub> phase, whose Pt<sub>2</sub>Te<sub>2</sub> layers can then act as the nuclei for the transformation into the pure Pt<sub>2</sub>Te<sub>2</sub> phase.

While the formation enthalpies explain why upon loss of Te from a PtTe<sub>2</sub> bilayer a Pt<sub>3</sub>Te<sub>4</sub> phase is formed (note that to obtain Pt<sub>2</sub>Te<sub>3</sub> one would require at least a 3-layer thick sample), rather than a phase segregation into pure Pt<sub>2</sub>Te<sub>2</sub> and PtTe<sub>2</sub> regions, it does not explain why once Pt<sub>3</sub>Te<sub>4</sub> is formed, it remains stable at temperatures around 350°C and does not continue to lose tellurium. To understand this apparent thermal stability of Pt<sub>3</sub>Te<sub>4</sub>, we investigate the Te-vacancy formation energies  $E_{vac}$  of the different phases, see SI for details, which is a measure for the thermal desorption of Te and thus the thermal stability of the phases. In Fig. 4(b),  $E_{vac}$  are plotted

as functions of Te chemical potential for the different phases in bilayer form. As evident from the plot, for a given value of Te-chemical potential,  $E_{\text{vac}}$  is considerably smaller for the PtTe<sub>2</sub> bilayer than for other phases. This is consistent with the observation that at low annealing temperatures (350°C) only the PtTe<sub>2</sub> regions desorb Te, and the regions that have transformed into the Pt<sub>3</sub>Te<sub>4</sub> are more stable towards further Te-loss. We also note that at all annealing temperatures Te and Pt adatoms are expected to be highly mobile, as, e.g., migration barrier of Pt adatom on both PtTe<sub>2</sub> (see SI) and MoS<sub>2</sub><sup>26</sup> are less than 0.5 eV. The analysis of the electronic structure (as detailed in SI) indicates that the values of  $E_{\text{vac}}$  are governed by charge transfer between the subsystems and the positions of the vacancy-induced states with respect to the Fermi energy  $E_{\text{F}}$ . Qualitatively this could be understood as follows: in metallic systems, if the spatially-localized defect-induced states are below  $E_{\text{F}}$ , they will be filled by electrons thus reducing the total energy of the system. In the single-particle picture (non-interacting electrons), the energy reduction will simply be the energy difference between the defect-induced states and  $E_{\text{F}}$ . We note that interlayer charge transfer modifies the electronic structure in Pt-Te systems and thus  $E_{\text{F}}$ , so that  $E_{\text{vac}}$  depends on the composition and electronic properties also of the adjacent layer and not just the properties of the layer in which the vacancy is formed. In calculations for a finite periodic supercell with a vacancy, which corresponds to a periodic array of defects, formation of a vacancy should also decrease  $E_{\text{F}}$ . The mechanism can be illustrated by the reduction of  $E_{\text{vac}}$  in the PtTe<sub>2</sub> bilayer with regard to the single-layer structure, Figs. S5 and S6. Isolated single-layer PtTe<sub>2</sub> structure is semiconducting with a band gap of about 0.4 eV. Formation of a Te vacancy gives rise to the empty states in the band gap, as evident from Fig. S6(a). Upon bilayer formation, the system becomes metallic, Fig. S6(b) and the vacancy-induced states are filled, Fig. S6(c), which gives rise to a decrease in  $E_{\text{vac}}$ . Density of states for the Pt<sub>2</sub>Te<sub>2</sub>/PtTe<sub>2</sub> system is shown in Fig. S7(a). Vacancy-induced states are strongly hybridized with the extended states, but the decrease in  $E_{\text{F}}$  is evident. Note also that there is no charge transfer into defect-induced states upon heterostructure formation, Fig. S7(b), as both subsystems are metallic.

The dependence of the chalcogen-vacancy formation energies in metallic vdW heterostructures on the adjacent layers illustrates another aspect of modifications of vdW-layer properties by

interlayer interactions. Specifically, it shows that the  $\text{Pt}_3\text{Te}_4$  phase cannot be described just as the combinations of the properties of  $\text{PtTe}_2$  and  $\text{Pt}_2\text{Te}_2$ , as it has different thermal stability. Importantly, the increased stability of the  $\text{PtTe}_2$  vdW-layer in the  $\text{Pt}_3\text{Te}_4$  structure, as compared to pure  $\text{PtTe}_2$  phase, enables the synthesis of  $\text{Pt}_3\text{Te}_4$  by the thermal Te-desorption procedure. We note that although the values of  $E_{\text{vac}}$  can be correlated with the stability of the systems, they cannot be used for the estimation of the concentration of defects in these systems in our experiments, as the system is likely not in equilibrium after annealing.

*Electronic structure:* The synthesis of the specific phases has also been confirmed by band structure measurements using ARPES and its comparison with band structure calculations by DFT. ARPES is enabled by the epitaxial growth of the films on  $\text{MoS}_2$  single crystals as demonstrated by the LEED pattern shown in Fig. 1(d). Fig. 5 shows ARPES data for  $\text{PtTe}_2$ ,  $\text{Pt}_3\text{Te}_4$ , and  $\text{Pt}_2\text{Te}_2$  systems obtained for the as grown, after annealing at  $350^\circ\text{C}$  for 450 min (plateau region) and after annealing at  $400^\circ\text{C}$  for additional 450 min, respectively. Band structure calculations for bilayers of the three Pt-telluride phases are also shown in Fig. 5 (a-f) as an overlay on the experimental data. It is noteworthy that although  $\text{Pt}_3\text{Te}_4$  is structurally composed of  $\text{PtTe}_2$  and  $\text{Pt}_2\text{Te}_2$  layers, the band structure is distinct and cannot be understood just by a combination of the electronic structure of these two phases, thus further illustrating the importance of the interlayer interactions in the Pt-telluride system. The overlay of the electronic structure calculations with the experimental band structure shows generally a good agreement, confirming the synthesis of these three phases. A discrepancy is found for  $\text{Pt}_2\text{Te}_2$ , which predicts the hole band at  $\Gamma$  to be  $\sim 380$  meV below the Fermi-level, while experimentally the band is only  $\sim 50$  meV below the Fermi level. This band is mainly derived from Te-*p* states and thus it is strongly influenced by Te-Te contacts at the interlayer. Pushing this band up in energy may suggest stronger interlayer contacts, induced by strain in the film or a slight variation of the interlayer separation on the experiment compared to those in the DFT calculations. A summary of the structural properties (lattice constants and interlayer separations) together with calculated band structures can be found in Fig. S8.

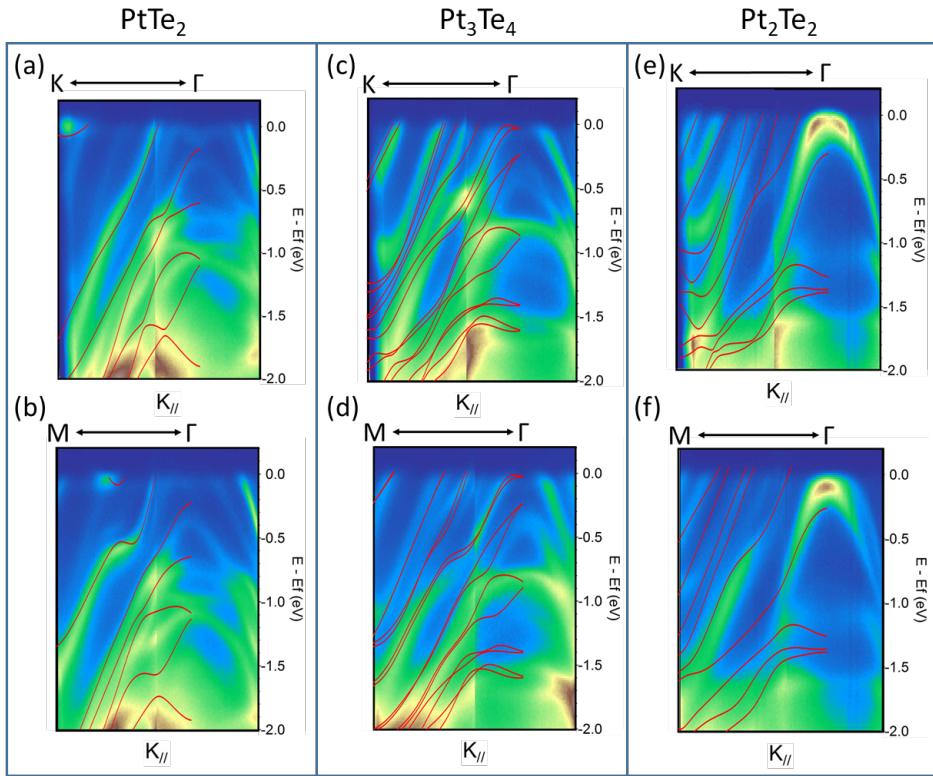


*Fig. 5: Phase dependent ARPES maps along  $\Gamma$ -K and  $\Gamma$ -M direction measured for  $\text{PtTe}_2$  (a,b),  $\text{Pt}_3\text{Te}_4$  (c,d) and  $\text{Pt}_2\text{Te}_2$  (e,f) phases. ARPES data was superimposed with the calculated band structure (red, solid lines), at DFT/PBE level including spin-orbit coupling.*

*Scanning tunneling microscopy:* To gain further nanoscale information about the transformation process from  $\text{PtTe}_2$  to the other phases, we performed detailed STM studies. It should be noted that all the different phases have a hexagonal surface unit cell with very similar lattice constants, which makes a distinction between the different phases using STM challenging. However, some variations in the film thickness and variations in the atomic-corrugation and defect concentrations are observed for different phases, and this allows to gain additional insight into the transformation processes and film morphologies during and after the transformation. The small height variation observed in the STM images for the different phases is illustrated in Figs. 6 (a) and (b). The sample shown in Fig. 6 has been prepared by short annealing (30 min) at 350°C of an initial  $\text{PtTe}_2$  film. After this annealing procedure predominantly bilayer  $\text{PtTe}_2$  is expected to be present with some conversion to  $\text{Pt}_3\text{Te}_4$ . In large-scale STM images shown in Fig. 6 (a) it is apparent that the bilayer terraces exhibit regions with a slight contrast variation. Fig. 6 (b) shows

two regions with increased contrast compared to the bilayer  $\text{PtTe}_2$  terraces. The corresponding line profile shows that these areas are only  $\sim 0.1$  nm and  $\sim 0.2$  nm taller than the  $\text{PtTe}_2$ . We interpret these two regions as  $\text{Pt}_3\text{Te}_4$  (i.e., a  $\text{Pt}_2\text{Te}_2$  on top or below the  $\text{PtTe}_2$  layer) and the slightly taller small island as a  $\text{Pt}_2\text{Te}_2$  island. The latter is extremely rare in these short-term annealed samples and is only chosen here as an indicator for the height differences in STM of these three different phases. Also note that the high-resolution inset of this  $\text{Pt}_2\text{Te}_2$  island embedded in  $\text{PtTe}_2$  indicates brighter edge states, suggesting possible undercoordinated edge sites. Importantly, point defects are imaged on the island, which are characteristic for  $\text{Pt}_2\text{Te}_2$ , as is discussed below.

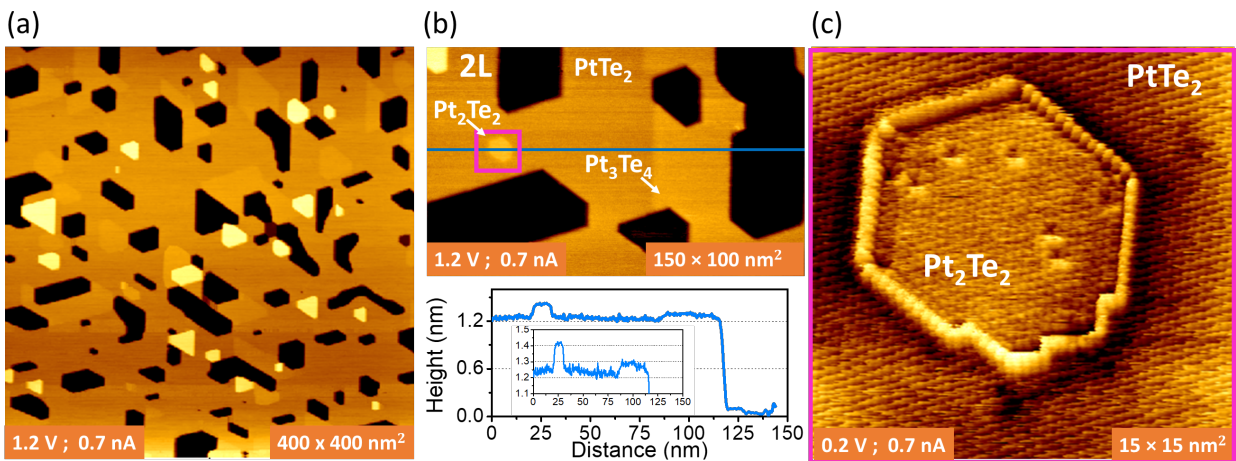


*Fig. 6: STM images illustrating height contrasts between different bilayer thick Pt-telluride phases. (a) large scale image of a sample annealed at 350°C for 30 min. The sample is primarily bilayer with some brighter tri-layer islands. The bilayer thick film exhibits regions with slightly different contrast. These contrast differences are shown in (b) where the line scan indicates step heights of only  $\sim 0.1$  nm and  $\sim 0.2$  nm between  $\text{PtTe}_2$  and regions associated with  $\text{Pt}_3\text{Te}_4$  and  $\text{Pt}_2\text{Te}_2$  bilayer regions, respectively. (c) small scale image of a  $\text{Pt}_2\text{Te}_2$  area embedded into  $\text{PtTe}_2$  bilayer film.*

For the  $\text{Pt}_3\text{Te}_4$  phase, two stacking orders are possible for a bilayer film, *i.e.*, a  $\text{PtTe}_2$  layer on top of  $\text{Pt}_2\text{Te}_2$  or vice versa, as schematically illustrated in Fig. 7. These two options cannot be distinguished from step heights at phase boundaries alone, but it would be important to know if there is a preferred stacking order in the transformed films. Since STM is primarily sensitive to the topmost surface, a  $\text{Pt}_3\text{Te}_4$  phase that is terminated with a  $\text{PtTe}_2$  layer may exhibit less of a

difference to a pure  $\text{PtTe}_2$  phase than a  $\text{Pt}_3\text{Te}_4$  phase terminated with a  $\text{Pt}_2\text{Te}_2$  layer. Small changes in the atomic imaging contrasts along boundaries and contrast differences along the phase boundaries shown in Fig. 7 suggest that both stacking orders are present for  $\text{Pt}_3\text{Te}_4$  regions and thus there is no clear preference for the termination of the bilayer  $\text{Pt}_3\text{Te}_4$  in our samples. For completeness, the boundary contrast along a  $\text{PtTe}_2/\text{Pt}_2\text{Te}_2$  boundary is also shown in Fig. 7. Similar to the data presented in Fig. 6, such a boundary shows a much better defined atomically sharp edge separating the two phases. The  $\text{Pt}_2\text{Te}_2$  phase also again shows a high density of point defects that are not present in either  $\text{PtTe}_2$  or  $\text{Pt}_3\text{Te}_4$ . These point defects are dark depressions with a triangular shape and are at positions where the bright atomic-scale protrusions would be for the  $\text{Pt}_2\text{Te}_2$  lattice. Simulated STM images indicate that protrusions in atomically resolved STM images correspond to surface Te-atoms for  $\text{Pt}_2\text{Te}_2$  and thus the observed defect is likely associated with a Te-vacancy. Simulations for both Te- and Pt- vacancies are shown in comparison to the experiments in Fig. S9. Both defects show depressions but obviously only the Te-vacancy is centered on the Te-sublattice and thus the Pt-vacancy defects can be excluded as the origin for the observed point defects. Consequently, these defects are ascribed to Te-vacancies. Bilayer  $\text{Pt}_2\text{Te}_2$  has the largest Te-vacancy formation energy for any of the phases studied here, and thus a high density of vacancies in this phase may be surprising. However, the  $\text{Pt}_2\text{Te}_2$  phase has already the lowest Te-concentration and cannot transform further to another phase with an even lower Te-concentration. Thus Te-vacancies cannot be annihilated by phase transformation and must remain as vacancies. Point defects in Pt-dichalcogenides have been studied extensively<sup>27</sup> and Pt vacancies have been identified as the locus of magnetic moments.<sup>28</sup> In the case of  $\text{Pt}_2\text{Te}_2$ , the DFT simulations do not exhibit spin-polarized states as shown in Fig. S9 and thus are unlikely to exhibit magnetic properties.

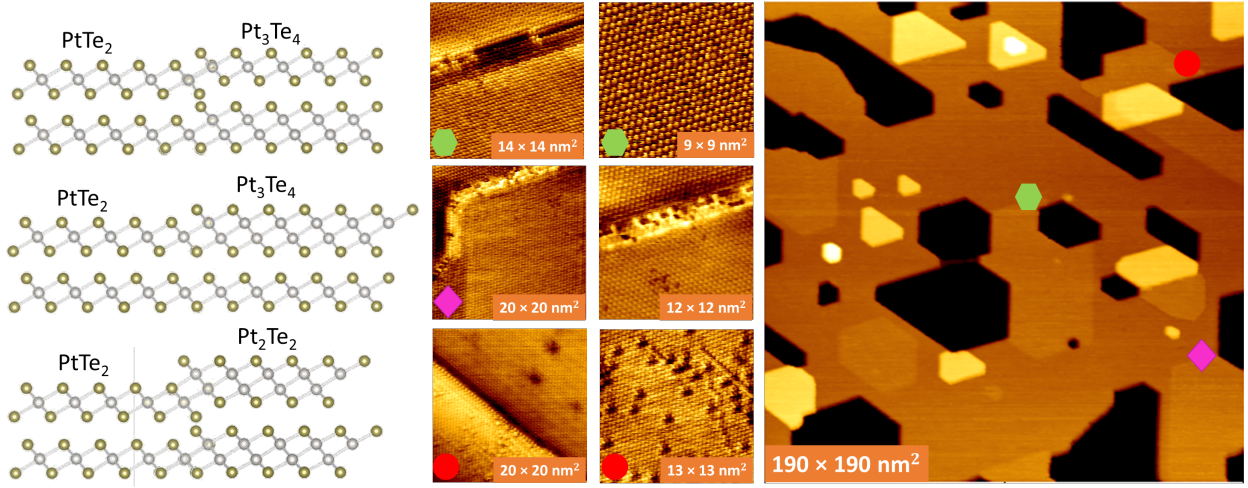


*Fig. 7: STM comparison of phase boundaries between  $\text{PtTe}_2$  and  $\text{Pt}_3\text{Te}_4$  or  $\text{Pt}_2\text{Te}_2$  domains. The left panel schematically illustrates the possible boundaries between the different compositional phases. The colored symbols of the high-resolution images indicate where these images were taken within the large-scale image on the right.*

Annealing at 400°C transforms the film from predominantly  $\text{Pt}_3\text{Te}_4$  phase to a  $\text{Pt}_2\text{Te}_2$  phase. This gives rise to a phase coexistence of these two phases. STM images of such phase coexistence are shown in Fig. 8. In large-scale images shown in Fig. 8(a), the two phases can be again distinguished by their small height contrast. At the atomic scale, the higher defect concentration (Te-vacancies) in  $\text{Pt}_2\text{Te}_2$  also allows differentiation between the two phases as shown in Fig. 8(b) and (c). The phase boundaries between  $\text{Pt}_2\text{Te}_2$  and  $\text{Pt}_3\text{Te}_4$  are atomically sharp.

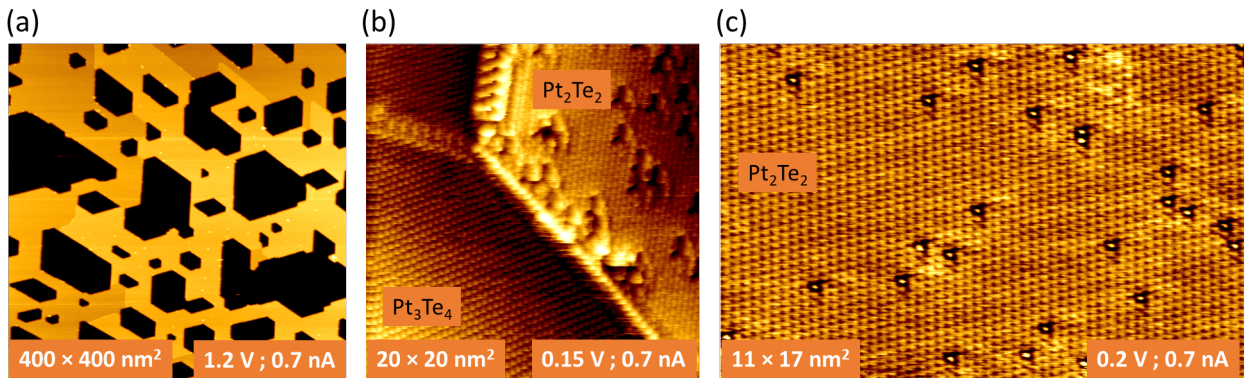


*Fig. 8: STM characterization of a  $\text{Pt}_3\text{Te}_4/\text{Pt}_2\text{Te}_2$  phase mixture. (a) Large scale image of a sample annealed at 350°C for 450 min followed by annealing at 400°C for another 150 min. (b) Atomically*

*resolved images presenting distinct difference between Pt<sub>3</sub>Te<sub>4</sub> and Pt<sub>2</sub>Te<sub>2</sub> bilayer regions. (c) Small scale image resolving point defects in Pt<sub>2</sub>Te<sub>2</sub> bilayer region. The point defects are centered on the Te-lattice (bright protrusions in atomic resolved STM images), thus making Te-vacancies the likely origin of these point defects. Note that the bright centers for the point defects are not usually observed and thus are likely STM-tip related artifact in this image.*

The STM characterization of the transformation from PtTe<sub>2</sub> to Pt<sub>3</sub>Te<sub>4</sub> and subsequently to Pt<sub>2</sub>Te<sub>2</sub> thus allows to reach the following conclusions: (i) The transformation occurs in bilayers. (ii) The transformation occurs by a nucleation and growth of the Te-deficient phase within the Te-rich phase, *i.e.*, Pt<sub>3</sub>Te<sub>4</sub> grows within the PtTe<sub>2</sub> phase and Pt<sub>2</sub>Te<sub>2</sub> grows within the Pt<sub>3</sub>Te<sub>4</sub> phase. (iii) For the Pt<sub>3</sub>Te<sub>4</sub> bilayers both structures with PtTe<sub>2</sub> in the surface layer and Pt<sub>2</sub>Te<sub>2</sub> in the bottom layer and *vice versa* are observed. (iv) Coexistence of Pt<sub>2</sub>Te<sub>2</sub> with PtTe<sub>2</sub> phase is rare. (v) The PtTe<sub>2</sub> and Pt<sub>3</sub>Te<sub>4</sub> phases have relatively low defect concentrations (Te-vacancies) as compared to the Pt<sub>2</sub>Te<sub>2</sub> phase. The low concentration of Te-vacancies in PtTe<sub>2</sub> and Pt<sub>3</sub>Te<sub>4</sub> suggests that Te-vacancies in these phases diffuse to the island edges, where these vacancies can be annihilated and liberate Pt-atoms that are then incorporated into the Te-deficient phase. This implies a high enough mobility of Te-vacancies and liberated Pt-atoms to diffuse to the growth front of the Te-deficient phases during the annealing process.

*Reversibility of conversion by Te-exposure:* Thermal annealing induced Te-loss allows the transformation of the film into bilayer Pt<sub>2</sub>Te<sub>2</sub>. A natural question is if this process can be reversed and the more thermodynamically stable PtTe<sub>2</sub> vdW layers can be regained by reacting these films with Te. To test this, we expose the Pt<sub>2</sub>Te<sub>2</sub> sample to Te at the same temperature and Te-flux that was used to grow the initial PtTe<sub>2</sub> sample in the MBE chamber. Figure 9(a), (b) and (c) shows large scale STM images of the sample before Te exposure, after exposing it for one hour, and after exposing for an additional hour to Te vapor at 200 °C. The area of the surface covered by Pt-telluride does not change significantly with Te-exposure, but investigation of the layer height, shown by the line profiles in the STM images in Fig. 9, indicate that the Pt-telluride islands have increased from the initially bilayer thick Pt<sub>2</sub>Te<sub>2</sub> islands with an apparent height of ~1.2 nm to

predominantly tri-layer height islands with an apparent height of  $\sim$ 1.8 nm. After the first Te-exposure (Fig. 9 (b)) both bi-layer and tri-layer height islands are observed, but after the second exposure almost exclusively tri-layer islands remain (Fig. 9(c)). To obtain information about the composition of the film, we performed XPS analysis. The Te:Pt atomic ratio changes from  $\sim$ 1 (using the calibration factors described above) to 1.6, *i.e.* close to an atomic ratio of 3:2 after Te-exposure. Moreover, the Pt-4f peaks shown in Fig. 9(d)-(e), transform from a single Pt-4f doublet for the initial  $\text{Pt}_2\text{Te}_2$  film to two doublets after Te-exposure. The peak positions of the two doublets are consistent with those described above for  $\text{PtTe}_2$  and  $\text{Pt}_2\text{Te}_2$ . The measured intensity ratio at normal emission angle of the  $\text{PtTe}_2:\text{Pt}_2\text{Te}_2$  components after 2h of Te exposure is  $\sim$ 1.9. This ratio depends, however, on the electron emission angle and increases with increasing emission angle (measured from the surface normal), as shown in Fig. 9 (f). The emission angle dependence is consistent with a structure that has the  $\text{Pt}_2\text{Te}_2$  layer further away from the surface than the  $\text{PtTe}_2$  layer(s), *i.e.*, emission from  $\text{Pt}_2\text{Te}_2$  is attenuated in surface sensitive XPS measurements.

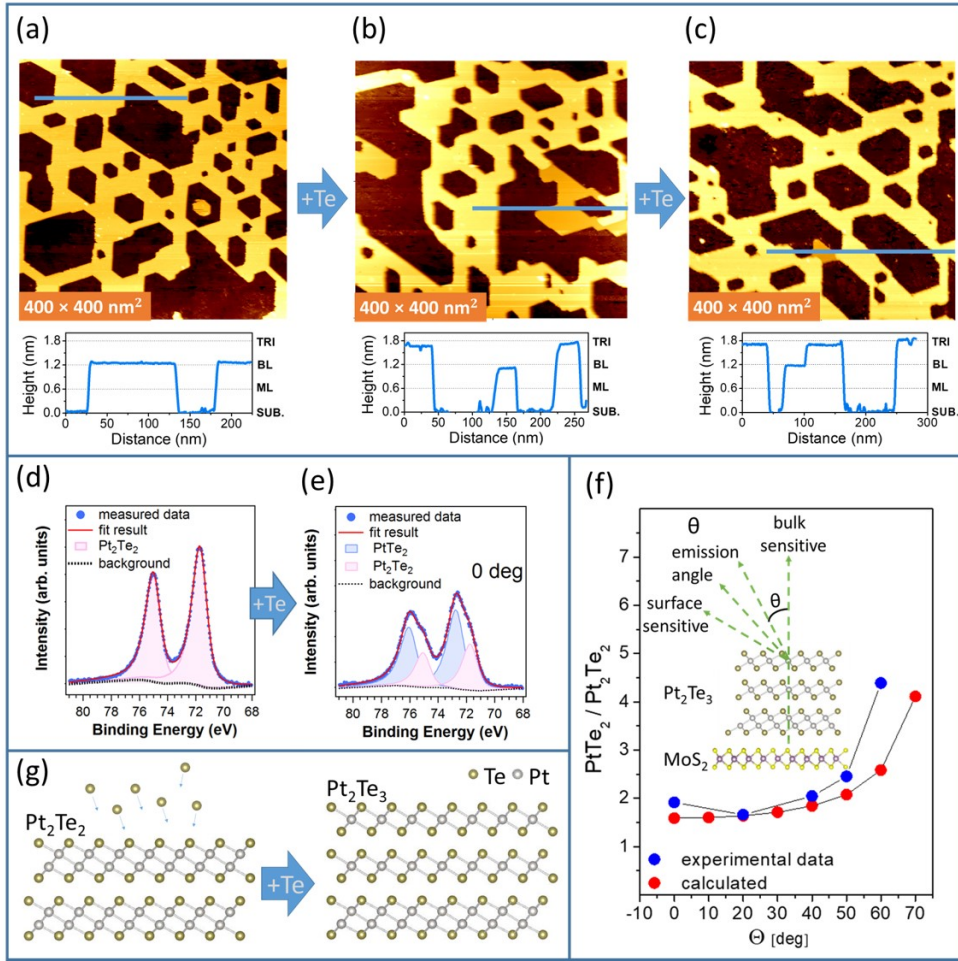


*Fig. 9: STM and XPS characterization of a Te exposed  $\text{Pt}_2\text{Te}_2$  bilayer. (a) Large scale image of a  $\text{Pt}_2\text{Te}_2$  sample with bilayer height islands. (b-c) STM images of the film exposed to Te-flux at 200°C for 1h and 2h, respectively. After exposure to Te-flux the coverage of the sample does not change significantly, but the island height increases to trilayers, as seen in the line profile. After an additional 1h exposure to Te, the majority of the sample is completely transformed into trilayer islands. Comparison of the XPS Pt-4f peaks of as prepared (d) and Te exposed (e) Pt-telluride film, indicates the film transformation from pure  $\text{Pt}_2\text{Te}_2$  to a sample containing both  $\text{Pt}_2\text{Te}_2$  and  $\text{PtTe}_2$ . XPS measurements as a function of electron emission angle shown in (f) show that the  $\text{Pt}_2\text{Te}_2$  component originates from a lower layer while the surface is  $\text{PtTe}_2$ . The measured intensity ratios and the angle dependence of the intensity ratio of the components is consistent with 2 layers of  $\text{PtTe}_2$  on top of a single layer  $\text{Pt}_2\text{Te}_2$ , i.e., a  $\text{Pt}_2\text{Te}_3$  film composition, as shown by the calculated expected component ratios for such a trilayer structure (Fig. S11). A schematic model of the*

*proposed film transformation is presented in panel (g) that illustrates that the topmost Pt<sub>2</sub>Te<sub>2</sub> layer is transformed into two PtTe<sub>2</sub> layers upon Te-exposure.*

From the observed change in layer thickness from a bilayer van der Waals structure to a trilayer van der Waals structure, the measured Te:Pt ratio and the observation of two Pt-4f components consistent with PtTe<sub>2</sub> and Pt<sub>2</sub>Te<sub>2</sub>, with the latter further away from the surface, we conclude that bilayer Pt<sub>2</sub>Te<sub>2</sub> transforms its surface layer into two PtTe<sub>2</sub> layers upon exposure to Te, while the bottom Pt<sub>2</sub>Te<sub>2</sub> remains unaltered. This transformation by Te-exposure is schematically illustrated in Fig. 9 (g). Such a structure is also consistent with the Pt-4f XPS intensity ratios for the Pt<sub>2</sub>Te<sub>2</sub> and PtTe<sub>2</sub> components. As shown in detail in Fig. S10 and S11, assuming a mean free electron path of ~ 2 nm and a layer thickness of ~0.6 nm of the individual van der Waals layers, one may estimate an intensity ratio for Pt<sub>PtTe2</sub>:Pt<sub>Pt2Te2</sub> of ~ 1.6 at normal electron emission for the proposed trilayer structure, which is in good agreement with the measurements.

The trilayer structure with one layer of Pt<sub>2</sub>Te<sub>2</sub> and two layers of PtTe<sub>2</sub> is the repeat unit of the thermodynamically stable Pt<sub>2</sub>Te<sub>3</sub> phase, Fig. 4 (a). The thermodynamic stability of this phase may aid its synthesis as an ultrathin film. However, it is likely that kinetic barriers for Te-diffusion into the lower Pt<sub>2</sub>Te<sub>2</sub> layer also plays an important role to only transform the surface layer. Regardless of the transformation mechanism, the reaction of Te with just the topmost layer of a bilayer PtTe<sub>2</sub> enables the formation of Pt<sub>2</sub>Te<sub>3</sub> films with the ultimate film thickness of only a single repeat unit. Thus, we demonstrated that all known vdW Pt-telluride compounds can be synthesized in their ultrathin form, which only consists of a single repeat unit of their bulk structure (with the exception of pure Pt<sub>2</sub>Te<sub>2</sub> which we only obtain as bilayers, although their structural/compositional repeat unit would be a single layer).

## Conclusions

Chalcogen desorption from layered dichalcogenides has been shown previously for (post)transition metal dichalcogenides to cause phase changes.<sup>29,30,31,32,33</sup> Here, this approach has

been successfully employed to control the synthesis of three different Pt-telluride phases with varying Pt:Te ratios. However, while in other systems the existence of only two stable layered vdW compounds was reported and thus desorption of chalcogens would naturally transform one phase to another, the existence of multiple phase compositions in the Pt-telluride system made the controlled synthesis of intermediate phases uncertain. Here we showed that the combination of favorable formation enthalpies of different phases and their Te-vacancy formation energies are responsible for enabling the synthesis of ultrathin films with single phase compositions. Specifically, the formation of the intermediate  $\text{Pt}_3\text{Te}_4$  phase is aided by its thermodynamically lower enthalpy of formation compared to a phase segregation into phase-pure  $\text{PtTe}_2$  and  $\text{Pt}_2\text{Te}_2$  bilayers and an increased thermal stability with respect to Te loss compared to  $\text{PtTe}_2$  bilayer phases, which causes a self-terminating transformation at low annealing temperatures ( $\sim 350^\circ\text{C}$ ). Raising the temperature then allows further transformation by Te-loss into  $\text{Pt}_2\text{Te}_2$ , similar to the single step transformations observed in some other vdW systems.<sup>31-33</sup> Interestingly, re-tellurization of bilayer  $\text{Pt}_2\text{Te}_2$  allows for the formation of  $\text{Pt}_2\text{Te}_3$  by selective transformation of the surface layer of  $\text{Pt}_2\text{Te}_2$  into two layers of  $\text{PtTe}_2$ . This selective reaction of the surface layer is likely a consequence of kinetic barriers for Te to diffuse to deeper layers.

While films with phase mixtures are often accidentally obtained by direct growth methods, we have demonstrated procedures for the single-phase synthesis of all known (meta)stable Pt-telluride vdW materials ( $\text{PtTe}_2$ ,  $\text{Pt}_2\text{Te}_3$ ,  $\text{Pt}_3\text{Te}_4$ , and  $\text{Pt}_2\text{Te}_2$ ) in their ultrathin form by exploiting a combination of thermodynamic and kinetic properties of these materials. In this work we established the transformation processes on the example of MBE grown films, however, it is expected that the same processes are universally applicable to any  $\text{PtTe}_2$  films or exfoliated flakes. Moreover, while in this study the entire film has been transformed by uniform heating of the sample, it is plausible that local heating can be used to convert area selected regions and thus allow lateral patterning of the Pt-telluride film into different phases. Generally, the controlled synthesis of materials in particular as thin films are the foundation for fundamental properties and to utilize them in applications. Consequently, the processes developed here, and the

scientific understanding of the mechanism involved lay the foundation for future studies and applications of the Pt telluride system.

## Methods

**Film growth and thermal treatment:** Platinum is evaporated from a 2 mm Pt-rod inside a water-cooled mini e-beam evaporator. Tellurium is heated in a Knudsen cell. The Te:Pt flux ratio, as determined from deposition rates on a microbalance, is about 10:1. PtTe<sub>2</sub> films are grown with a MoS<sub>2</sub> single crystal substrate held at 200 °C and with a slow growth rate of ~3 ML/h, where the growth rate is estimated from surface coverage in scanning tunneling microscopy images (STM) and a monolayer (ML) is defined as a single PtTe<sub>2</sub> layer. Subsequent to the vacuum characterization of the film by STM, LEED, XPS, and ARPES, the film is annealed to a target temperature in vacuum and held at this temperature for a period of time. Initial target temperature was set to 350 °C which was increased to 400 °C after the film reached a Pt<sub>3</sub>Te<sub>4</sub> composition. The annealing periods are shown in Figs. 2 and 3. After each annealing step the samples are again characterized by the above-mentioned vacuum surface science techniques.

**XPS/peak fitting:** XPS measurement were performed in the analysis chamber equipped with a Scienta R3000 hemispherical energy analyzer and non-monochromatized dual anode x-ray source. The spectra collected here were Al-K<sub>α</sub> radiation. Te-3d and Pt-4f spectra were collected after each annealing step. The Pt-4f peaks were fit with two doublets corresponding to Pt in a PtTe<sub>2</sub> and Pt<sub>2</sub>Te<sub>2</sub> environment. Prior to the peak fitting a Shirley-background was subtracted. The peak shape (Lorentzian-Gaussian mixture, peak asymmetry, and full-width-half maximum) for the two Pt-components was determined for the pure PtTe<sub>2</sub> (as grown) and Pt<sub>2</sub>Te<sub>2</sub> (after annealing to 400 °C for 400 min) by optimizing the fit to reduce the residual. These fits indicate binding energies for Pt-4f<sub>5/2</sub>/ Pt-4f<sub>7/2</sub> of 76.19 eV / 72.86 eV and 75.01 eV / 71.68 eV for the PtTe<sub>2</sub> and Pt<sub>2</sub>Te<sub>2</sub>-phase, respectively. The Pt<sub>3</sub>Te<sub>4</sub> phase is fit with two doublets and is determined by fixing the peak shapes to those determined to the two pure phases, i.e., Pt in Pt<sub>2</sub>Te<sub>2</sub> environment and Pt in a PtTe<sub>2</sub> environment, but let the peak position freely adjust to minimize the residual. This fitting procedure resulted in peak positions for Pt-4f<sub>5/2</sub> at 75.01 eV and 75.93 eV for Pt<sub>2</sub>Te<sub>2</sub> and PtTe<sub>2</sub> components respectively, indicating that the PtTe<sub>2</sub> component in Pt<sub>3</sub>Te<sub>4</sub> is shifted by ~ 0.3 eV to higher binding energy compared to the binding energy of the pure PtTe<sub>2</sub> phase. For mixed phases the peak positions are free to adjust while the peak shapes are kept fixed. With this fitting the peak intensity

*ratios for Pt in a  $\text{PtTe}_2$  and Pt in a  $\text{Pt}_2\text{Te}_2$  environment are determined, which is plotted in Fig. 3 (c).*

**ARPES:** ARPES was conducted using a re-focused He-discharge lamp generating He-I radiation with a beam energy of 21.2 eV. The same electrostatic analyzer as for XPS was used to determine the band dispersion. All the measurements were taken for epitaxial Pt-telluride films grown on a  $\text{MoS}_2$  single crystal substrate and the crystallographic directions were determined by LEED. All measurements were acquired with the sample at room temperature.

**STM:** All STM images were acquired using a room temperature Omicron STM-1 microscope. Electrochemically etched tungsten tips, which were sputter-cleaned in vacuum, were used as STM probes.

**DFT:** Spin-polarized density functional calculations were carried out using the Vienna ab-initio Simulation Package (VASP).<sup>34,35</sup> The Perdew–Burke–Ernzerhof (PBE)36 exchange–correlation functional was used for structural optimization and electronic structure calculations. The force tolerance of  $0.01 \text{ eV } \text{\AA}^{-1}$  and electronic convergence criteria of  $10^{-5} \text{ eV}$  was chosen for the relaxation of the structures. The energy cut-off was set to 600 eV. The Brillouin zone of the slabs and bulk systems was sampled using  $12 \times 12 \times 1$  and  $12 \times 12 \times 12$  k-points, respectively. Defective bilayer systems are modeled with  $5 \times 5$  supercells. The Brillouin zone of the systems was sampled by using a  $3 \times 3 \times 1$  Gamma-centered k-point grid. Van der Waals (vdW) interactions were taken into account using the many-body dispersion (MBD) combined with fractional ionic atoms method (FIA) as implemented by Tawfik *et al.*<sup>37</sup> The effect of spin-orbit coupling (SOC) is included in all the electronic structure calculations. Charge transfer between the bilayer materials was assessed via calculating the Bader charge difference between the combined system and isolated monolayers. The formation enthalpies of the systems are estimated with respect to the elemental chemical potentials ( $\mu$ ) of the components Pt and Te (taken as their lowest energy bulk structures).

#### **Supporting Information:**

The supporting information is available free of charge at: <http://pubs.acs.org/doi/XXXXXXX>

Fig S1: STM bias dependence of moiré pattern in monolayer  $\text{PtTe}_2$ .

Fig S2: Pt-4f XPS analysis of film conversion as function of annealing time and temperature.

Fig S3: Te-3d XPS analysis of film conversion as function of annealing time and temperature.

Fig. S4: Exponential decay fitting parameters of XPS data shown in Fig. 3.

Fig. S5: Vacancy formation energies  $E_{\text{vac}}$  for various Pt-Te systems calculated with and without account for vdW interaction.

Fig. S6: Calculated density of states (DOS) of single- and bi- layer  $\text{PtTe}_2$  with and without Te vacancy.

Fig. S7: Calculated density of states (DOS) of  $\text{Pt}_2\text{Te}_2/\text{PtTe}_2$  structures with and without single Te vacancy in the  $\text{Pt}_2\text{Te}_2$  layer.

Fig. S8: Calculated band structure for various Pt-telluride bilayers.

Fig. S9: Calculated point defects in  $\text{Pt}_2\text{Te}_2$  and comparison to STM data.

Fig. S10 and S11: Structural model of  $\text{Pt}_2\text{Te}_3$  and corresponding estimation of take-off angle dependent Pt-4f component intensity ratio.

**Acknowledgment:** Financial support from the National Science Foundation under award 2140038 is acknowledged. In addition, we acknowledge funding from the German Research Foundation (DFG), project KR 4866/6-1, and through the collaborative research center “Chemistry of Synthetic 2D Materials” SFB-1415-417590517. We further thank the Gauss Centre for Supercomputing e.V. ([www.gauss-centre.eu](http://www.gauss-centre.eu)) for providing computing time on the GCS Supercomputer HAWK at Höchstleistungsrechenzentrum Stuttgart ([www.hlrs.de](http://www.hlrs.de)) and also TU Dresden (Taurus cluster) for generous grants of CPU time.

## References:

- 
- 1 Lasek, K.; Li, J.; Kolekar, S.; Coelho, P.M.; Guo, L.; Zhang, M.; Wang, Z.; Batzill, M. Synthesis and Characterization of 2D Transition Metal Dichalcogenides: Recent Progress from a Vacuum Surface Science Perspective. *Surf. Sci. Rep.* **2021**, *76*, 100523.
- 2 Lin, M.-K.; Villaos, R.A.B.; Hlevyack, J.A.; Chen, P.; Liu, R.-Y.; Hsu, C.-H.; Avila, J.; Mo, S.-K.; Chuang, F.-C.; Chiang, T.C. Dimensionality-Mediated Semimetal-Semiconductor Transition in Ultrathin PtTe<sub>2</sub> Films. *Phys. Rev. Lett.* **2020**, *124*, 036402.
- 3 Li, J.; Kolekar, S.; Ghorbani-Asl, M.; Lehnert, T.; Biskupek, J.; Kaiser, U.; Krasheninnikov, A.V.; Batzill, M. Layer-Dependent Band Gaps of Platinum Dichalcogenides. *ACS Nano* **2021**, *15*, 13249–13259.
- 4 Villaos, R.A.B.; Crisostomo, C.P.; Huang, Z.-Q.; Huang, S.-M.; Padama, A.A.B.; Alba, M.A.; Lin, H.; Chuang, F.-C. Thickness Dependent Electronic Properties of Pt Dichalcogenides. *npj 2D Mater. Appl.* **2019**, *3*, 2.
- 5 Miró, P.; Ghorbani-Asl, M.; Heine, T. Two Dimensional Materials Beyond MoS<sub>2</sub>: Noble-Transition-Metal Dichalcogenides. *Angew. Chem. Int. Ed.* **2014**, *53*, 3015–3018
- 6 Zhang, L.; Yang, T.; Arramel; Feng, Y.P.; Wee, A.T.S.; Wang, Z. MBE-Grown Ultrathin PtTe<sub>2</sub> Film and the Layer-Dependent Electronic Structure. *Nanoscale* **2022**, accepted manuscript doi: 10.1039/D2NR00944G
- 7 Yan, M.; Huang, H.; Zhang, K.; Wang, E.; Yao, W.; Deng, K.; Wan, G.; Zhang, H.; Arita, M.; Yang, H.; Sun, Z.; Yao, H.; Wu, Y.; Fan, S.; Duan, W.; Zhou, S. Lorentz-Violating Type-II Dirac Fermions in Transition Metal Dichalcogenide PtTe<sub>2</sub>. *Nat. Commun.* **2017**, *8*, 257.
- 8 Fujii, J.; Ghosh, B.; Vobornik, I.; Sarkar, A.B.; Mondal, D.; Kuo, C.-N.; Bocquet, F.C.; Zhang, L.; Boukhvalov, D.W.; Lue, C.S.; Agarwal, A.; Politano, A. Mitrofanovite Pt<sub>3</sub>Te<sub>4</sub>: A Topological Metal with Termination-Dependent Surface Band Structure and Strong Spin Polarization. *ACS Nano* **2021**, *15*, 14786–14793.
- 9 Xu, H.; Wei, J.; Zhou, H.; Feng, J.; Xu, T.; Du, H.; He, C.; Huang, Y.; Zhang, J.; Liu, Y.; Wu, H.-C.; Guo, C.; Wang, X.; Guang, Y.; Wei, H.; Peng, Y.; Jiang, W.; Yu, G.; Han, X. High Spin Hall Conductivity in Large-Area Type-II Dirac Semimetal PtTe<sub>2</sub>. *Adv. Mater.* **2020**, *32*, 2000513.
- 10 Pavlosiuk, O.; Kaczorowski, D. Galvanomagnetic Properties of the Putative Type-II Dirac Semimetal PtTe<sub>2</sub>. *Sci. Rep.* **2018**, *8*, 11297.
- 11 Politano, A.; Chiarello, G.; Kuo, C.-N.; Lue, C. S.; Edla, R.; Torelli, P.; Pellegrini, V.; Boukhvalov, D. W.; Tailoring the Surface Chemical Reactivity of Transition-Metal Dichalcogenide PtTe<sub>2</sub> Crystals. *Adv. Funct. Mater.* **2018**, *28*, 1706504
- 12 Chia, X.; Adriano, A.; Lazar, P.; Sofer, Z.; Luxa, J.; Pumera, M. Layered Platinum Dichalcogenides (PtS<sub>2</sub>, PtSe<sub>2</sub>, and PtTe<sub>2</sub>) Electrocatalysis: Monotonic Dependence on the Chalcogen Size. *Adv. Funct. Mater.* **2016**, *26*, 4306–4318.
- 13 Rosli, N.F.; Mayorga-Martinez, C.C.; Latiff, N.M.; Rohaizad, N.; Sofer, Z.; Fisher, A.C.; Pumera, M. Layered PtTe<sub>2</sub> Matches Electrocatalytic Performance of Pt/C for Oxygen Reduction Reaction with Significantly Lower Toxicity. *ACS Sustain. Chem. Eng.* **2018**, *6*, 7432–7441.
- 14 Wang, Y.; Li, Y.; Heine, T. PtTe Monolayer: Two-Dimensional Electrocatalyst with High Basal Plane Activity toward Oxygen Reduction Reaction. *J. Am. Chem. Soc.* **2018**, *140*, 12732–12735.

- 
- 15 Likforman, A.; Carre, D.; Etienne, J; Bachet, J. Structure Cristalline du Monoseleniure Indium InSe. *Acta Cryst.* **1975**, *31*, 1252-1254.
- 16 Kuhn, A.; Chevy, A.; Chevalier, R. Crystal Structure and Interatomic Distances in GaSe. *Phys. Status Solidi A* **1975**, *31*, 469-475.
- 17 Wang, H.-C.; Botti, S.; Marques, M.A.L. Predicting Stable Crystalline Compounds using Chemical Similarity. *npj Comp. Mater.* **2021**, *7*, 12.
- 18 Soled, S.; Wold, A.; Gorochov, O. Crystal Growth and Characterization of Platinum Ditelluride. *Mater. Res. Bull.* **1975**, *10*, 831-835.
- 19 Thomassen, L. Ueber Kristallstrukturen einiger Binaerer Verbindungen der Platinmetalle. *Z. Physik. Chem. B* **1929**, *2*, 349-379.
- 20 Gimpl, M. L.; Nelson, C. E.; Fuschillo, N. Some Properties of Platinum Monotelluride (PtTe). *Amer. Mineral.* **1963**, *48*, 689–691.
- 21 Stolyarova, T.A.; Osadchii, E.G. Enthalpy of Formation of Platinum and Palladium Monotellurides from the Elements. *Geochem. Internat.* **2013**, *51*, 852–854.
- 22 Cenzual, K.; Gelato, L.M.; Penzo, M.; Parthé, E. Overlooked Triagonal Symmetry in Structures Reported with Monoclinic Centered Bravais Lattices, Trigonal Description of Li<sub>8</sub>Pb<sub>3</sub>, PtTe, Pt<sub>3</sub>Te<sub>4</sub>, Pt<sub>2</sub>Te<sub>3</sub>, LiFe<sub>6</sub>Ge<sub>4</sub>, LiFe<sub>6</sub>Ge<sub>5</sub>, CaGa<sub>6</sub>Te<sub>10</sub>, and La<sub>3.266</sub>Mn<sub>1.1</sub>S<sub>6</sub>. *Zeitschr. Kristallogra.* **1990**, *193*, 217-242.
- 23 Subbotin, V.V.; Vymazalová, A.; Laufek, F.; Savchenko, Y.E.; Stanley, C.J.; Gabov, D.A.; Plášil, J. Mitrofanovite, Pt<sub>3</sub>Te<sub>4</sub>, a New Mineral from the East Chuarvy Deposit, Fedorovo–Pana Intrusion, Kola Peninsula, Russia. *Mineral. Mag.* **2019**, *83*, 523 – 530.
- 24 Tang, J.; Chang, L.-T.; Kou, X.; Murata, K.; Choi, E. S.; Lang, M.; Fan, Y.; Jiang, Y.; Montazeri, M.; Jiang, W.; Wang, Y.; He, L.; Wang, K. L. Electrical Detection of Spin-Polarized Surface States Conduction in (Bi<sub>0.53</sub>Sb<sub>0.47</sub>)<sub>2</sub>Te<sub>3</sub> Topological Insulator. *Nano Lett.* **2014**, *14*, 5423–5429.
- 25 Böker, T.; Severin, R.; Müller, A.; Janowitz, C.; Manzke, R.; Voß, D.; Krüger, P.; Mazur, A.; Pollmann, J. J. P. R. B., Band structure of MoS<sub>2</sub>, MoSe<sub>2</sub>, and α– MoTe<sub>2</sub>: Angle-resolved photoelectron spectroscopy and ab initio calculations. *Phys. Rev. B* **64**, 235305 (2001).
- 26 Wu, P.; Yin, N.; Li, P.; Cheng, W.; Huang, M. The adsorption and diffusion behavior of noble metal adatoms (Pd, Pt, Cu, Ag and Au) on a MoS<sub>2</sub> monolayer: a first-principles study. *Phys. Chem. Chem. Phys.* **2017**, *19*, 20713-20722.
- 27 Li, J.; Joseph, T.; Ghorbani-Asl, M.; Kolekar, S.; Krasheninnikov, A.V.; Batzill, M. Edge and Point-Defect Induced Electronic and Magnetic Properties in Monolayer PtSe<sub>2</sub>. *Adv. Funct. Mater.* **2022**, 2110428
- 28 Avsar, A.; Ciarrocchi, A.; Pizzochero, M.; Unuchek, D.; Yazyev, O.V.; Kis, A. Defect Induced, Layer-Modulated Magnetism in Ultrathin Metallic PtSe<sub>2</sub>. *Nat. Nanotechnol.* **2019**, *14*, 674–678.
- 29 Arnold, F.; Stan, R.-M.; Mahatha, S.K.; Lund, H.E.; Curcio, D.; Dendzik, M., Bana, H.; Travaglia, E.; Bignardi, L.; Lacovic, P.; Lizzit, D.; Li, Z.; Bianchi, M.; Miwa, J.A.; Bremholm, M.; Lizzit, S.; Hofmann, P.; Sanders, C.E. Novel Single-Layer Vanadium Sulphide Phases. *2D Mater.* **2018**, *5*, 045009.
- 30 Liu, Z.-L.; Lei, B.; Zhu, Z.-L.; Tao, L.; Qi, J.; Bao, D.-L.; Wu, X.; Huang, L.; Zhang, Y.-Y.; Lin, X.; Wang Y.-L.; Du, S.; Pantelides, S.T.; Gao H.-J. Spontaneous Formation of 1D Pattern in Monolayer VSe<sub>2</sub> with Dispersive Adsorption of Pt Atoms for HER Catalysis. *Nano Lett.* **2019**, *19*, 4897–4903.
- 31 Sutter, E.; Huang, Y.; Komsa, H.-P.; Ghorbani-Asl, M.; Krasheninnikov, A.V.; Sutter, P. Electron-Beam Induced Transformations of Layered Tin Dichalcogenides. *Nano Lett.* **2016**, *16*, 4410–4416.

- 
- 32 Li, J.; Kolekar, S.; Xin, Y.; Coelho, P.M.; Lasek, K.; Nugera, F.A.; Gutiérrez, H.R.; Batzill, M. Thermal Phase Control of Two-Dimensional Pt-Chalcogenide (Se and Te) Ultrathin Epitaxial Films and Nanocrystals. *Chem. Mater.* **2021**, *33*, 8018-8027.
- 33 Zhu, H.; Wang, Q.; Zhang, C.; Addou, R.; Cho, K.; Wallace, R.M.; Kim, M.J. New Mo<sub>6</sub>Te<sub>6</sub> Sub-Nanometer-Diameter Nanowire Phase from 2H-MoTe<sub>2</sub>. *Adv. Mater.* **2017**, *29*, 1606264.
- 34 Kresse, G.; Hafner, J. *Ab Initio* Molecular Dynamics for Liquid Metals. *Phys. Rev. B* **1993**, *47*, 558(R).
- 35 Kresse, G.; Furthmüller, J. Efficient iterative schemes for ab initio total-energy calculations using a plane-wave basis set. *Phys. Rev. B* **1996**, *54*, 11169-11186.
- 36 Perdew, J.P.; Burke, K.; Ernzerhof, M. Generalized Gradient Approximation Made Simple. *Phys. Rev. Lett.* **1996**, *77*, 3865.
- 37 Tawfik, S.A.; Gould, T.; Stampfl, C.; Ford, M.J. Evaluation of van der Waals Density Functionals for Layered Materials. *Phys. Rev. Mater.* **2018**, *2*, 034005.